Egypt. J. Chem. **Vol. 68**, No. 2. pp. 75 – 89 (2025)

Egyptian Journal of Chemistry

http://ejchem.journals.ekb.eg/

Enhancing Corrosion Behavior of T91 Steel in 3.5% NaCl through Graphene Oxide Nanocomposite Coatings

Ghalia A. Gaber[1], Lamiaa Z. Mohamed[2], Gehad Hamdy[1]

[1] Chemistry Department, Faculty of Science, Al-Azhar University (Girls), Yousef Abbas Str., Nasr City, P.O. Box: 11754, Cairo, Egypt.

[2] Mining, Petroleum, and Metallurgical Engineering Department, Faculty of Engineering, Cairo University, Giza, ١٢٦١٣, Egypt

Abstract

In various industries, the susceptibility of T91 steel to corrosion often necessitates the adoption of highly efficient surface coatings. Despite significant interest in developing a stable, cost-effective, and efficient graphene coating for T91 steel, achieving this goal has been challenging. To address this, electrodeposition was employed to apply Ni-reduced graphene doped with Ni/GO/TiO_2 and GO/Fe-TiO_2 nanocomposite coatings onto T91 steel substrates. Notably, the graphene nanocomposite coatings formed strong bonds with the T91 steel surface via Cr-C bonding, ensuring exceptional durability. Gravimetric, potentiodynamic polarization (PP), and cyclic voltammetry (CYV) experiments were conducted to evaluate the coatings' electrochemical response in a 3.5% NaCl solution. The Ni/GO/Fe-TiO_2 coating exhibited a corrosion rate (CR) of 0.854 mm/y on T91 steel at room temperature, markedly lower than the untreated T91 steel CR of 2.321 mm/y. The method outlined in this study for producing graphene doped nanocomposite coated on the T91 steel is straightforward. The properties of deposition-coated surfaces were determined using XRD, SEM, and EDX analysis. Optimization studies are crucial in coating systems, with ANOVA being a commonly employed statistical technique. RSM was utilized to optimize the corrosion rate of T91 steel, measured using the weight loss method. Additionally, response optimization for CR identified a maximum fit of 74.39% after 24 h, with a weight loss of 0.00513 for Ni/GO/Fe-TiO_2. The predicted R^2 (97.55%) and adjusted R^2 (99.25%) values are closely aligned, indicating the model's accuracy.

Keywords: T91 steel, Corrosion resistance, Nanocomposite coating, electrodeposition technique, Microstructure.

1. Introduction

Corrosion, a gradual and expected deterioration of steel structures, significantly impacts the economy [1, 2]. Effective corrosion management techniques can impede or delay this process [3, 4]. Shielding coatings, widely employed across various contexts, offer a practical means of protection, encompassing paints, galvanized layer films, or organic layers [5, 6, 7, 8, 9, 10]. However, the substantial depth of these coatings can alter the chemical and physical properties of the metals they protect, thereby diminishing their thermal and electrical conductivity. Moreover, organic coatings may allow the penetration of corrosive electrolytes onto the metal's surface underneath, leading to adhesion loss, cathodic delamination, and the generation of corrosive byproducts. These factors accelerate the degradation of the metal substrate [11]. Hence, reducing coating thickness while enhancing adhesion is crucial for developing effective anti-corrosive coatings. Steel grade 91 (T91), also known as 9Cr-1Mo-V steel, is a type of low alloy steel primarily used in high-temperature and high-pressure applications, particularly in power plants for components like boilers and piping systems. Piping systems in marine environments need to withstand corrosive seawater and high pressures. T91 steel's corrosion resistance and strength make it a viable option for piping systems, ensuring durability and reliability in marine conditions [12].

Since its inception in 2004, graphene has been composed of a single layer of hexagonal carbon atoms and has attracted considerable interest across numerous fields due to its vast potential applications. It is widely acknowledged that graphene acts as the fundamental building block of graphitic materials in all dimensions except one [13]. The tightly organized graphene's (two-dimensional (2D)) atomic structure allows it to produce a strong diffusion barrier (perfect impenetrability) against the movement of any atom or molecule. Theoretically, this may create a physical barrier that keeps corrosive species away from the metal below. Graphene also possesses other desirable qualities, such as strong electrical and thermal conductivities [14], special optical transparency [15, 16], as well as innate mechanical properties [17, 18]. When combined with its impermeability and chemical stability, graphene is recognized as a viable option for a new anticorrosion nanomaterial. Researchers around the world are diligently working to develop graphene coatings for metal substrates as thin, anticorrosion layers [19]. In general, by incorporating graphene nanosheets into a polymer matrix, graphene might be used as a protective covering on any metallic

*Corresponding author e-mail: lamiaa.zaky@cu.edu.eg ; (Lamiaa Z. Mohamed).
Receive Date: 30 April 2024, Revise Date: 07 June 2024, Accept Date: 25 June 2024
DOI: 10.21608/ejchem.2024.286273.9662

surface [11]. As an alternative, a graphene coating created by chemical vapor deposition (CVD) or wet transfer over Ni or Cu foil has exceptional antioxidation and anticorrosion properties in harsh conditions. The corrosion rate (CR) values of metals coated in graphene are notably lower than those of the original, uncoated metals [20, 21]. Despite early signs of success, several obstacles persist in the practical adoption of graphene anticorrosive coatings within the corrosion control field. A notable challenge has been the creation of high-quality graphene coatings directly on commercial steels and other alloys, such as magnesium and aluminum alloys. Furthermore, the typical CVD technique's growth temperature was around 1000 ºC, which was too high for steel and other alloys to tolerate and might have adverse effects including segregation and carburization during the process of cooling [22, 23]. Furthermore, neither CVD nor wet-transfer graphene coatings could offer high interfacial adhesion because of capillary forces and/or van der Waals. As a result, the metal substrate might be penetrated by the corrosive electrolyte [24, 25]. Furthermore, the application of coating with graphene may expedite the electrochemical corrosion process, as graphene's semi-metallic nature creates a battery circuit at the interface with the metal [26, 27].

Several investigations have examined the use of graphene or graphene oxide (GO) for protecting metals, yielding varying results. Raza et al. [28] demonstrated that NdFeB magnets coated with GO displayed improved corrosion resistance in a 0.6M NaCl solution. Behunová et al. [29], on the other hand, found that Cu electrophoretically coated with GO showed approximately 6 times reduction in corrosion rate compared to uncoated Cu. In contrast, Park et al. [30] investigated GO coatings produced by electrophoretic deposition (EPD) on mild steel and found no significant impact on its corrosion properties. Kirkland et al. [31] assessed graphene coatings' corrosion performance relative to the underlying substrate and concluded that the effectiveness varied depending on the metal substrate. Concerns persist regarding the anti-corrosive efficacy of GO coatings on mild steel, underscoring the need for further research to gain a comprehensive understanding of their anti-corrosion properties.

The study successfully employed the electrodeposition approach to deposit a layer of Ni-reduced graphene doped with Ni/GO/TiO_2 and Ni/GO/Fe-TiO_2 onto the surface of T91 steel. Throughout the electrodeposition process, the graphene sheets were uniformly deposited onto the surface of T91 using the electrochemical deposition method. It was observed that the graphene layer could react with the T91 substrate, leading to the formation of Cr_xC_y due to the "mechanochemical effect," with chromium being the predominant element in the steel for carbide generation. Subsequently, the T91 surface continued to receive graphene coatings due to the presence of mechanical force and/or strong van der Waals force. Figure 1 illustrates the relevant schematic of the preparation procedure. Thus, the graphene doped nanocomposite coated on the T91 steel served as a model system to evaluate the corrosion-resistant properties. An investigation was conducted to assess the corrosion resistance of graphene in 3.5% NaCl using various electrochemical techniques. This study introduced a novel and straightforward approach for fabricating graphene doped nanocomposite coated on the T91 steel, demonstrating exceptional performance. A Ni-reduced graphene material was synthesized via electrodeposition, with the incorporation of Ni/GO/TiO_2 and Ni/GO/Fe-TiO_2 coatings. The corrosion behavior of this material was then examined in a 3.5% NaCl solution. Surface morphology analysis of the various coating baths was performed using scanning electron microscopy (SEM), while energy dispersive X-ray analysis (EDX) determined the elemental composition. Additionally, after corrosion occurred, SEM and EDX were employed to assess the corrosion products present on the coated T91 steel. The experiments for ANOVA analysis were designed and analyzed using the statistical software MINITAB 18.

2. Experimental work

2.1. Materials

The chemicals used in this experiment were obtained from Sigma Aldrich. Distilled water (DW) was utilized consistently throughout the experiment. Titanium tetraisopropoxide (TTIP), Hydrochloric acid (HCl), and 2-propanol were used to prepare nano-TiO_2. $NiSO_4.7H_2O$, Na_2SO_4, and H_3BO_3 were used for electrodeposition baths. Ammonia solution and sulfuric acid were used to adjust the bath pH. The GO was fabricated by modified Hummer's method as reported by M. Fathy et. al [32], GO/TiO_2 and GO/Fe-TiO_2 were prepared as reported in our previous work [33, 34]. A solution of NaCl from Sigma Aldrich was utilized for both chemical and electrochemical tests. A solution with a high pH, containing sodium hydroxide (NaOH), sodium carbonate (Na_2CO_3), and sodium phosphate (Na_3PO_4), was used for immersing the T91 steel to eliminate grease. The material utilized is steel grade 91 (T91). The chemical constituents are provided in Table 1. Five readings of the Vickers hardness were conducted using a 10 kg force for 10 seconds, and the average value was calculated. The mean Vickers hardness value is 206.

Table 1. The chemical constituents of T91 steel in wt.%.

C	Mn	Si	S	P	Cr	Ni	Mo	V	Ti	Nb
0.11	0.51	0.32	0.005	0.012	8.55	0.15	0.88	0.21	0.002	0.08

2.2. Preparation of nano-TiO_2

The nanopowder of TiO_2 was synthesized using the sol-gel method with titanium tetraisopropoxide (TTIP). To control the hydrolysis process, a small amount of hydrochloric acid (HCl) was added to 10 ml of 2-propanol to adjust the pH to 1.89. Gradually, 11.7 ml of TTIP was added to form the solution, followed by refluxing at 70°C. To produce nanoparticles, the solution was briefly heated after adding 11.5 ml of distilled water. The resulting gel was dried at 70°C for 16 h to remove the solvent through evaporation. Finally, the material underwent calcination at 500°C to yield nano-TiO_2 [35].

2.3. Electrodeposition process

The cathode utilized for obtaining coatings on T91 steel substrates has dimensions of 2×2×0.1 cm^3. An electrodeposition method was employed to fabricate coatings of nickel and its composites. The Ni bath consisted of $NiSO_4.7H_2O$ [26.26 gL^{-1}], Na_2SO_4 [56.81 gL^{-1}], and H_3BO_3 [18.54 gL^{-1}]. The utilizing coating bathes contain Ni, Ni/TiO_2, Ni/GO/TiO_2, and Ni/GO/Fe-TiO_2. The

electrodeposition process involved using Ti-7Cr-4Fe alloys as the anode and T91 steel as the cathode. Figure 1 illustrates a schematic diagram illustrating the electrodeposition procedure. The operating settings were as follows: a current density of 7 mA/cm², a temperature of 30°C, a pH of 5 (adjusted using an ammonia solution and sulfuric acid), a deposition period of 60 minutes, and a stirring speed of 150 rpm.

Before the electrodeposition process, several preparation procedures were carried out on the steel surface. The initial stage involved a mechanical procedure, using various grades of emery paper to achieve a smooth surface. The second step involved degreasing, where a solution containing NaOH, Na_2CO_3, and Na_3PO_4 was used to eliminate any grease, with the sample immersed in the solution for 5 minutes. After each procedure, the sample underwent thorough rinsing with deionized water and subsequent drying. Before electrodeposition, the deposition solution containing Ni/TiO_2, Ni/GO/TiO_2, and Ni/GO/Fe-TiO_2 was stirred for 2 h to ensure that the nanoparticles of Ni/TiO_2, Ni/GO/TiO_2, and Ni/GO/Fe-TiO_2 were uniformly distributed and well mixed in the solution.

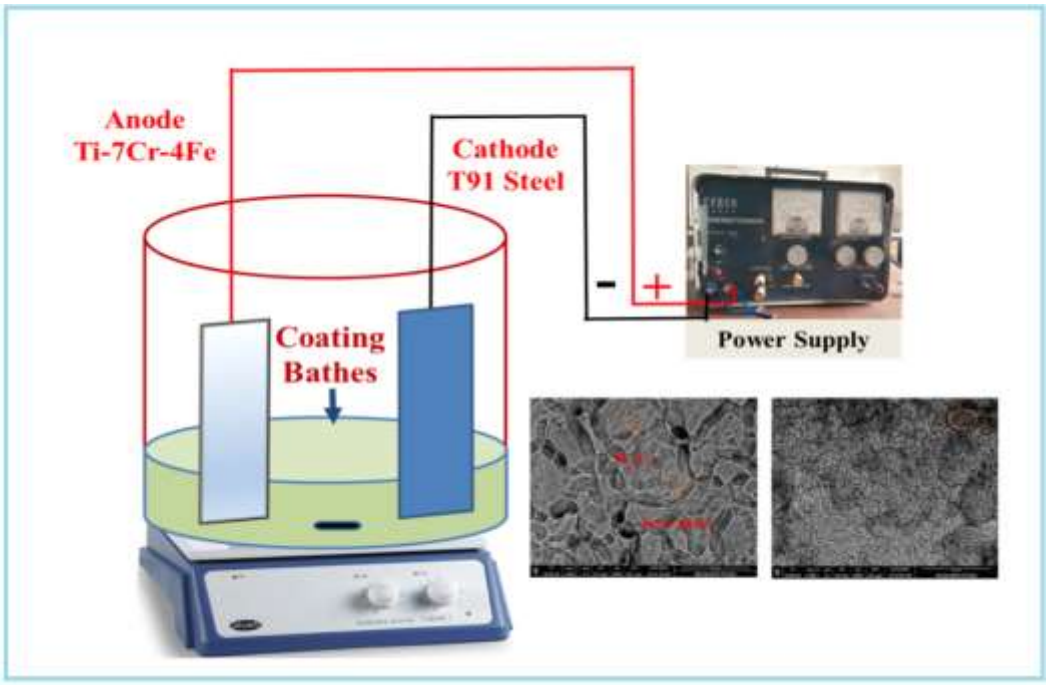

Fig. 1. Schematic representation of electrodeposition process for coatings on T91 steel.

2.4. Corrosion of T91 steel

Electrochemical studies were conducted using the Voltalab 40 Potentiostat PGZ301 (Germany) and Volta Master 4 software to measure and analyze corrosion. The four materials tested were Ni, Ni/TiO_2, Ni/GO/TiO_2, and Ni/GO/Fe-TiO_2 bathes which served as the working electrodes. A solution of sodium chloride (NaCl) with a concentration of 3.5% (purchased from Sigma Aldrich) was utilized for both chemical and electrochemical experiments.

The weight loss (WL) findings of T91 steel samples, after the deposition of nanoparticles, were tested in a 3.5% NaCl solution for 120 h. The T91 steel CR value, following the deposition of nanoparticles in a 3.5% NaCl using the WL technique at a temperature of 25°C, was determined using Eq. 1 [36, 37]:

$$\text{C.R. (mm/y)} = \frac{\Delta W \times K}{A \times T \times D} \qquad (1)$$

The equation incorporates several variables, each with specific definitions: K, a constant set at 8.76×10^4; T, denoting the exposure time in h; A, representing the area measured in cm^2; ΔW, indicating the mass loss in grams; and D, signifying the density in g/cm^3. The surface coverage (θ) was calculated using Eq. 2.

$$\theta = \frac{W_0 - W_i}{W_0} \qquad (2)$$

The Wi represents the WL value of T91 steel after nanoparticle deposition, while W_0 represents the WL value of T91 steel after treatment with a Ni bath. The percentage of inhibitory efficiency $IE\%$ is calculated using Eq. 3 [38]:

$$IE\% = \theta \times 100 \qquad (3)$$

Following that, potentiodynamic polarization (PP) plots were employed to assess both the corrosion current density and corrosion potential. The working electrode underwent a voltage sweep ranging from -0.6 to +0.1 V at a scanning rate of 2 mV/s. The inhibitory efficiency (IE %) was determined using Eq. 4:

$$IE = (1 - \frac{CR_{inh}}{CR_0}) \times 100 \qquad (4)$$

The CR_0 represents the CR value in the absence of the nanocomposite, while CR_{inh} represents the CR value when the nanocomposite is present.

Finally, T91 steel was subjected to cyclic voltammetry (CYV) experiments in chloride media in the absence/ presence of nanocomposite coating using a potentiostat model PGZ301. The potential was first measured at a cathodic direction and then allowed to sweep to an anodic direction until a sharp change in the current's direction in the active direction was seen. After that, a second cathodic sweep of the sample was performed. In this study, electrochemical measurements and immersion tests of the specimens were conducted at room temperature (RT) under ambient exposure conditions.

2.5. Morphology of Corroded T91 steel

A surface morphology analysis was performed on the corroded alloy before and after applying a coating. The SEM used for inspection is manufactured by FEI and located in the southern region of the Netherlands. It is equipped with EDX and a Bryker AXS flash detector from Germany.

2.6. Statistical Analysis

Analysis of variance (ANOVA) is a statistical method used to determine if there are significant differences between the means of various observational groups by analyzing variance ratios. The planned model requires 20 runs, with some repetition in the middle of the trial run combinations. The experimental model is created randomly using the statistical program MINITAB 18, which generates the experimental worksheet based on the specified levels and factors.

3. Results and Discussion

3.1. Characterization of nano-TiO_2

The nano-TiO_2 was analyzed using Fourier transform infrared spectroscopy (FTIR) over the wavenumber range of 4000–400 cm^{-1} and X-ray diffraction (XRD) with CuKa radiation (λ = 1.5406 μm) [39]. In Figure 2a, the infrared spectrum of the synthesized nano-TiO2 is displayed. The presence of a band between 500 and 600 cm^{-1} indicates stretching vibrations in the Ti-O-Ti and Ti-O bonds [39]. XRD analysis of the nano-TiO_2, as described in Figure 2b, shows a prominent peak at 2θ, indicating the presence of the (101) plane of the anatase phase, confirming the successful preparation of nano-TiO_2 in the anatase phase. Additional peaks correspond to various planes of the anatase phase: (103), (004), (112), (200), (105), (211), (213), (204), and (116) [13]. The average size of the crystallites is determined using the Scherrer equation ($D = (K.\lambda)/(\beta*\cos\theta)$), yielding a result of 49.20 nm [40].

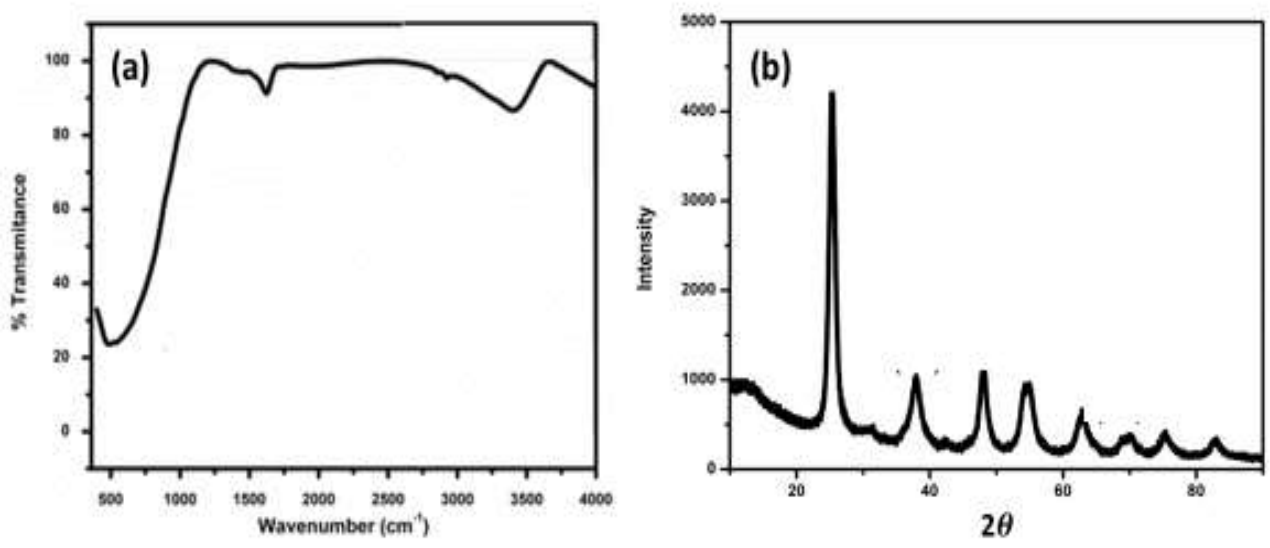

Fig. 2. Nano- TiO_2 (a) FTIR and (b) XRD pattern.

3.2 Coating characteristics

The SEM images and EDX results of different nanocomposite coating on T91 steel substrate are in Fig. 3 and Fig. 4, respectively. Fig. 3(a) represents the coating by Ni bath which coats the T91steel grain with a layer that appears with two phases M23C6 which is represented here Cr23C6 and the laves phase this is confirmed by EDX results in Fig. 4 (a) for the laves phase. nanocoat with Ni/TiO_2 in Fig. 3 (b) contains layers of two colors white gray and dark gray. The EDX analysis of the dark gray proves the presence of Ti, O, and Ni in the coating Fig. 4 (b). Fig. 3 (c) displays the covering of the nanocoat on the T91 surface which confirmed the existence of Ti, O, C, and Ni from EDX results in Fig. 4 (c). Finally, the nano-coating which is like a protective layer on the surface in Fig. 3 (d), confirmed by EDX analysis in Fig. 4 (d) the existence of Ti, O, C, and Ni. The oxygen percentage is the highest percentage from TiO_2, GO, and Fe_3O_4. The formation of pores in the film was affected by hydrogen evolution at cathodic sites. The dense and smooth coating detected in this study is likely recognized as the absence of intermetallic phases, which facilitates the creation of a uniform and barrier-type coating [41].

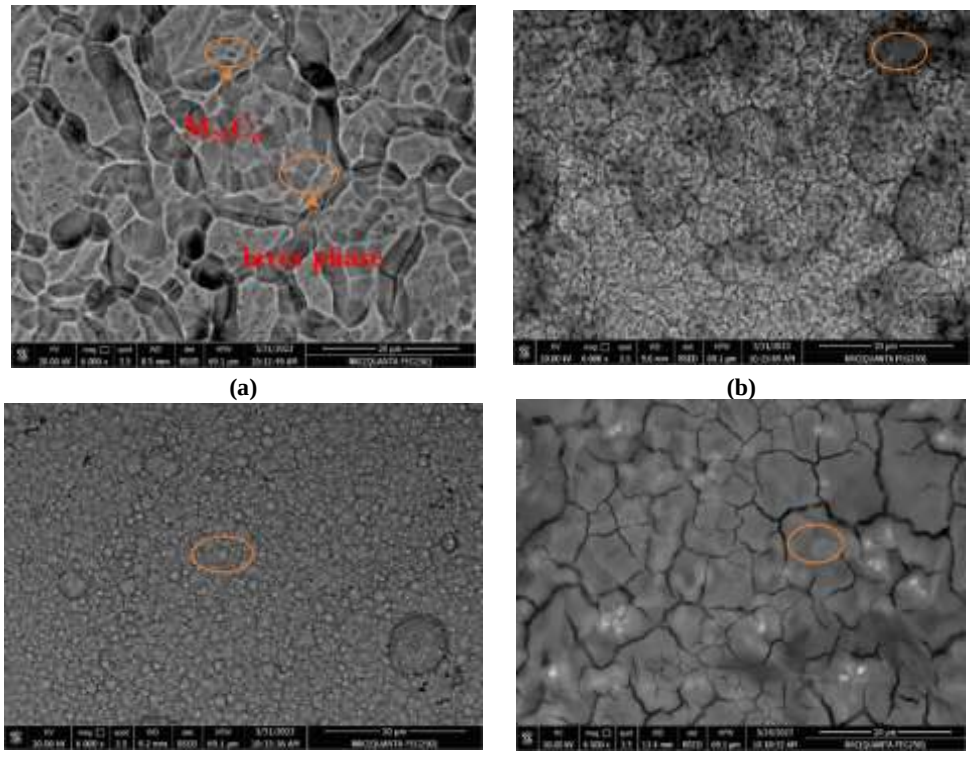

(a) **(b)**

(c) **(d)**

Fig. 3. The SEM images of T91 steel after coating by (a) Ni, (b) Ni/TiO_2, (c) Ni/GO/TiO_2, and (d) Ni/GO/Fe-TiO_2 bathes.

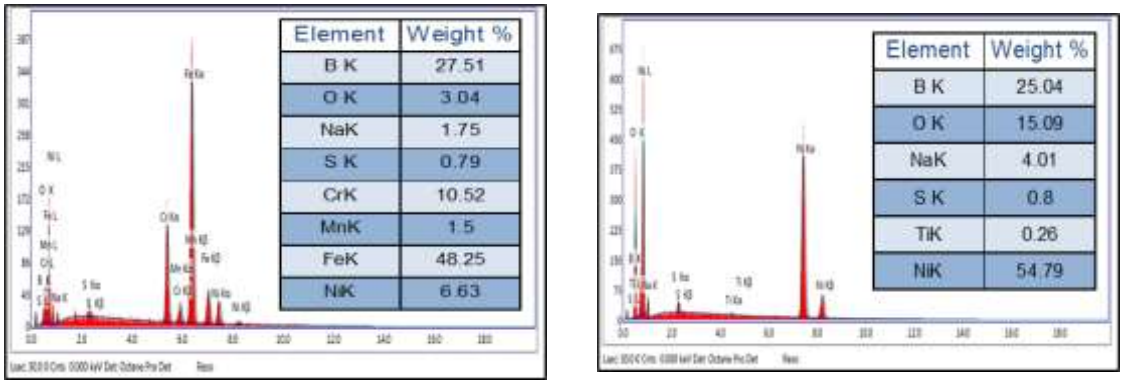

Element	Weight %
B K	27.51
O K	3.04
NaK	1.75
S K	0.79
CrK	10.52
MnK	1.5
FeK	48.25
NiK	6.63

Element	Weight %
B K	25.04
O K	15.09
NaK	4.01
S K	0.8
TiK	0.26
NiK	54.79

(a) **(b)**

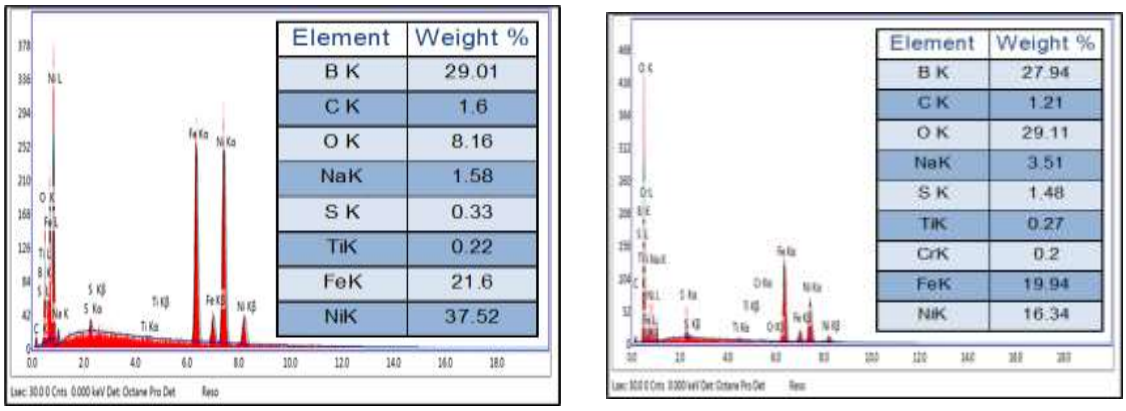

(c) **(d)**

Fig. 4. The EDX results of T91 steel after coating by (a) Ni, (b) Ni/TiO_2, (c) Ni/GO/TiO_2, and (d) Ni/GO/Fe-TiO_2 bathes

3.3. Gravimetric Measurement

Figure 5 illustrates the gravimetric data of the studied coating when immersed in 3.5% NaCl for up to 120 h. The evolution of the attack curve allows for a quantitative analysis of how time impacts the degradation of the metallic coating. Even after the immersion period, the corrosion resistance of untreated T91 steel remains significantly higher compared to all deposition coatings. Overall, all samples exhibit highly comparable performance. Concerning deposition coating, the WL values initially start at a low level and subsequently increase as the immersion period progresses. This indicates the presence of corrosion at the beginning of immersion, with subsequent CR values decreasing as the spaces between the hopeite crystals become filled with corrosion products.

When coated, the T91 steel demonstrates a moderate level of protection, with the Ni/GO/Fe-TiO_2 coating offering the highest level of protection. Regarding the kinetics of the process, during the initial immersion period, all four deposition coatings exhibit a moderate CR that decreases over time, indicating diffusion processes as the main factors controlling the CR. As immersion time rises, the surfaces of the samples develop a white layer of corrosion products, except for the Ni/GO/Fe-TiO_2 samples, which remain unaffected. This protective layer impedes the solution from reaching the metallic steel, resulting in no observable degradation in the Ni/GO/Fe-TiO_2 coating. Upon testing several coatings, it was noted that the WL remained relatively constant during the initial 72 h of immersion, suggesting that the CR remained nearly consistent over time, albeit slightly higher than that of the T91 steel. Subsequently, over up to 120 h, the deterioration of the coatings continued to progress in a nearly linear fashion. However, for the Ni/GO/Fe-TiO_2 coating, the rate of deterioration appeared to decrease.

The CR of untreated T91 steel in a 3.5% NaCl solution was determined to be around 2.461 mm/y based on the change in weight loss after immersing for 120 h, as shown in Table 2. However, the CR, determined by measuring the amount of mass lost from the deposition-coated Ni/GO/Fe-TiO_2, was found to be 0.5896 mm/y. Figure 6 illustrates the CR of T91 steel with nanocomposite deposition after it was submerged in 3.5% NaCl for 120 h. The rise in the CR of T91 occurred due to the system's progression towards the uncoated steel in this specific environment. This was evident from the significant presence of rust on the samples after the immersion test. The inverse relationship between R_p and CR suggests that the decrease in CR values with time reflects the presence of corrosion protection offered by the nanocomposite coating. Applying layers of compounds containing oxide and/or hydroxide on the metal surface enhances the oxygen concentration on the surface of the substrate, hence increasing its ability to donate electrons [42]. It is pertinent to note that about 76.0 % of inhibition could be achieved for a period of exposure of 120 h using Ni/GO/Fe-TiO_2 coating. The WL results show that GO coating prevents contact between corrosive medium and T91 steel, leading to corrosion resistance.

Table 2. The CR, the Inhibition efficiency (IE%), and Surface coverage (θ), of T91 steel with and without nanocomposite deposition in 3.5 % NaCl solution at 25°C.

Conditions	WL g	CR mm/y	θ	IE %
T91 Steel	0.1056	2.4613	--	--
Ni	0.0602	1.4031	0.429	42.9
Ni/TiO_2	0.0480	1.1187	0.545	54.5
Ni/GO/TiO_2	0.0390	0.9090	0.631	63.1
Ni/GO/Fe-TiO_2	0.0253	0.5896	0.760	76.0

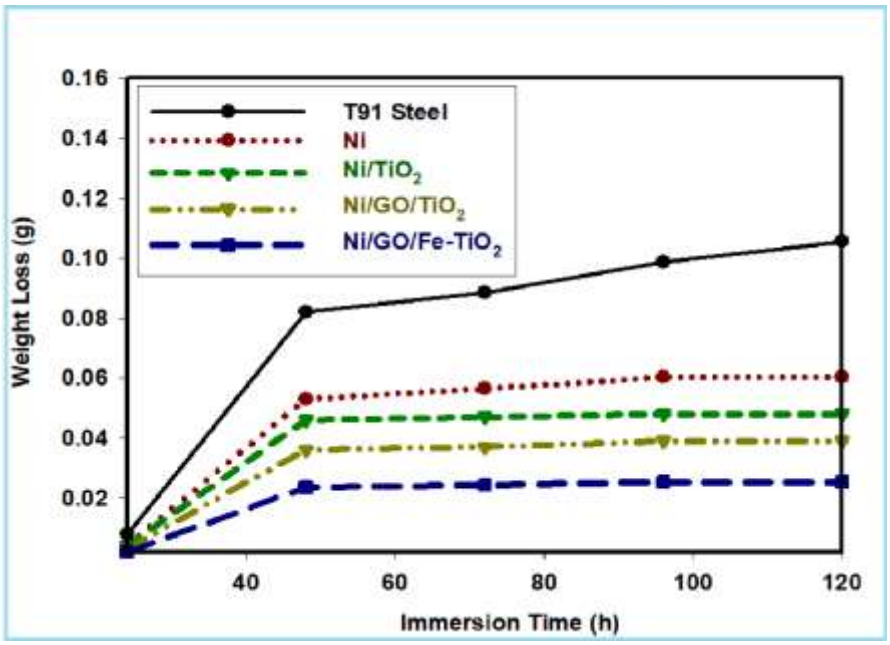

Fig. 5. The WL values of T91 steel after different nanocomposite coatings immersed in 3.5 % NaCl.

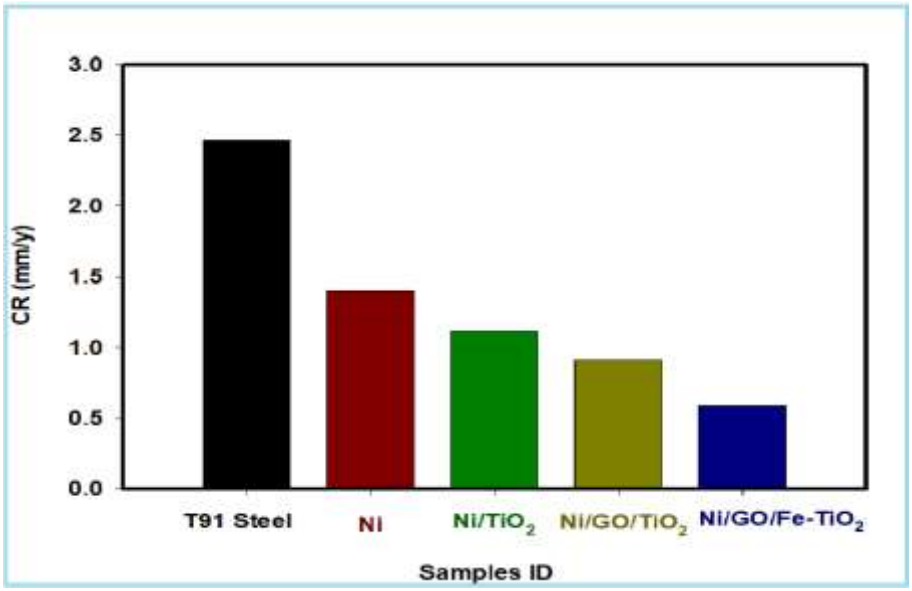

Fig. 6. The CR values of T91 steel after different nanocomposite coatings immersed in 3.5% NaCl for 120 h.

3.4. Electrochemical measurements

3.4.1. Potentiodynamic polarization measurements

Figure 7 illustrates the standard polarization plots for untreated T91 steel and T91 steel coated with a nanocomposite when immersed in 3.5% NaCl. The corrosion potential (E_{corr}), CR, and corrosion current density (I_{corr}), slopes of the anodic and cathodic Tafel lines (β_a and β_c) obtained from these curves are presented in Table 3. Polarization scanning was performed near the Tafel linear sections to determine the numerical values of the CR. The E_{corr} values for both untreated and coated samples range from -494.3 to -398.6 mV. Samples with the Ni/GO/Fe-TiO_2 coating exhibit higher E_{corr} values, indicating nobler behavior, whereas untreated T91 steel samples have more negative E_{corr} values. The inclusion of the Ni/GO/Fe-TiO_2 nanocomposite coating results in an approximate increase of 398.6 mV in E_{corr}, acting as a protective barrier. The CR decreases by 0.854 mm/y, with the level of enhancement surpassing or equaling that of Ni/TiO_2 and Ni/GO/TiO_2 nanocomposite coatings. Comparing the Rp variation of the Ni/GO/Fe-TiO_2 nanocomposite coating with other coatings reveals that the former exhibits greater values while the latter has lower values. The R_p values increase due to the filling of gaps between hopeite crystals by corrosion products. Subsequently, the motion of the electrolyte during measurements exposes the holes once more. This behavior aligns with changes in E_{corr} readings. The rise in E_{corr} can be attributed to the system's transition towards uncoated T91 steel in this specific environment, as indicated by the significant occurrence of rust on the samples at the test's conclusion [43].

The anodic branches reveal the disintegration of T91 steel and a continuous increase in current, indicating a reaction rate controlled by diffusion. Additionally, these branches demonstrate that various surface treatments resulted in an accelerated anodic dissolution rate compared to untreated T91 steel. This unexpected behavior could be attributed to the untreated sample's exposure to air and subsequent drying after immersion in 3.5% NaCl before PP tests. According to reports, allowing T91 steel material to naturally dry after immersion in a 3.5% NaCl significantly reduces the CR. This reduction is attributed to the formation of denser corrosion product films during the drying process [44]. Within the cathodic curves, a significant decrease in current density values is evident when comparing the untreated sample to the nanocomposite-coated sample. This reduction is precisely one order of magnitude, as confirmed by the I_{corr} values in Table 3, calculated using potentiostat software. It's worth noting that all surface conditions exhibit low I_{corr} values, and the anodic slope values decrease as the CR increases. The inhibitory effect of the nanocomposite coating is evident in the reduction of the oxygen reduction rate.

The insignificant corrosion concert of Ni/GO/TiO_2 may be attributed to the hydrophilic properties of GO and the compromised structure resulting from oxidation, which creates vulnerable spots for the corrosive electrolyte to infiltrate. In contrast, the Ni/GO/Fe-TiO_2 composite exhibited superior resistance to corrosion compared to the bare metal. Additionally, it significantly reduced the CR and caused a positive shift in the E_{corr}. Previous reports have indicated that the use of reduced graphene oxide (rGO) leads to the formation of a hydrophobic and more compact graphitic structure [45, 46]. This could perhaps explain the enhanced performance observed in the Ni/GO/Fe-TiO_2 system. Furthermore, Jin et al. [47] discovered that the thermal reduction of GO coatings enhances the adhesion of coatings by forming a chemical bond (C-O-Fe) between the metallic substrate and GO. This bond is created by the potential breakdown of C=O. The improved adhesion is likely the reason for the superior corrosion resistance noted in the Ni/GO/Fe-TiO_2 nanocomposite coating.

Table 3. The electrochemical parameters of the PP curves of T91 steel with and without nanocomposite deposition in a 3.5% NaCl.

Conditions	E_{corr} mV	I_{corr} mA/cm^2	β_a mV/dec	β_c -mV/dec	R_p Ωcm^{-2}	CR mm/y	IE %
T91 Steel	-494.3	0.198500	178.9	-117.0	97.61	2.321	--
Ni	-494.1	0.156245	146.7	-125.6	102.90	1.827	21.3
Ni/TiO_2	-479.5	0.114131	122.6	-173.8	106.45	1.334	42.5
Ni/GO/TiO_2	-468.2	0.091214	71.8	-76.8	147.41	1.066	54.1
Ni/GO/Fe-TiO_2	-398.6	0.072983	44.0	-56.5	403.66	0.854	63.2

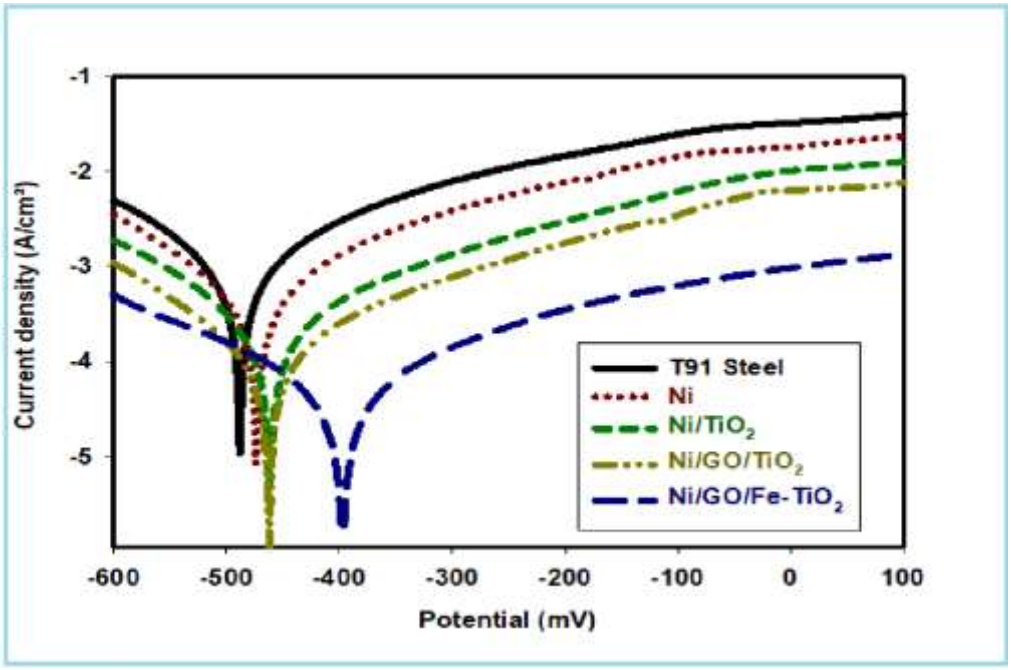

Fig. 7. The PP curves for T91 steel after different nanocomposite coatings immersed in 3.5 % NaCl.

3.4.2. Cyclic Voltammetry

Fig. 8 depicts the CYV curves for T91 steel after nanocomposite deposition immersed in 3.5 % NaCl. The CYV corrosion parameters such as E_{corr}, E_{pitt}, E_{prot}, CR, and I_{corr}, are listed in Table 4. Notably, the anodic current density for T91 steel decreases after the deposition of the nanocomposite. This suggests that the electro-oxidation processes of all coating are being inhibited.

The deposition with Ni/GO/Fe-TiO_2 nanocomposite exhibits consistent passive characteristics throughout a broad potential range. This is followed by a decrease in E_{corr} values towards more negative values in comparison to T91 steel. The incorporation of Ni/GO/Fe-TiO_2 led to the creation of the most effective coating, as demonstrated by the complete elimination of the hysteresis loop noted during the inverse anodic scan. This eradication served as an indication of the absence of pitting corrosion. Commonly, the CYV curves' hysteresis loop area immediately indicates localized corrosion. For instance, a large hysteresis loop area implies corrosion vulnerability. The reverse anodic scan shows a hysteresis loop, suggesting pitting. The passive surface pitting is caused by chloride ions competing for adsorption at the metal/oxide layer contact. At a certain chloride concentration, a pitting potential displaces oxygen from the protective oxide layer. This effect agrees with that observed by the PP measurements.

Table 4. The CYV parameters of T91 steel with and without nanocomposite deposition in 3.5 % NaCl.

Conditions	E_{corr} (mV/SCE)	I_{corr} (mA/cm²)	E_{pit} (mV/SCE)	E_{prot} (mV/SCE)	CR mm/y	IE %
T91 Steel	-373.5	0.16618	199.5	-364.5	1.943	--
Ni	-351.0	0.07887	193.5	-342.0	0.923	52.5
Ni/TiO_2	-353.6	0.06902	190.5	-349.5	0.807	58.5
Ni/GO/TiO_2	-357.0	0.06764	183.0	-345.0	0.791	59.3
Ni/GO/Fe-TiO_2	-327.7	0.03759	166.5	-321.0	0.439	77.4

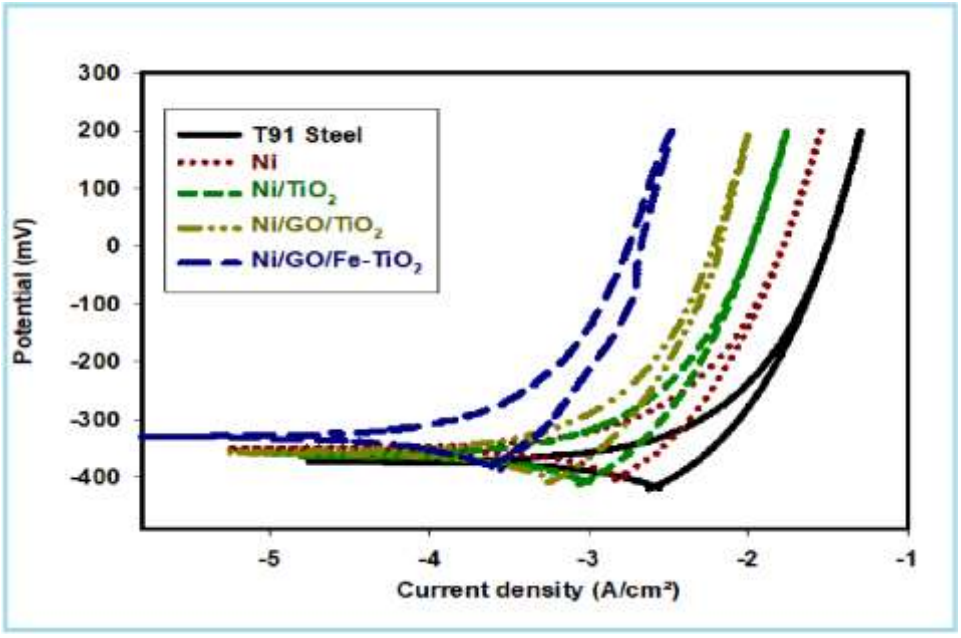

Fig. 8. The CYV curves for T91 steel after different nanocomposite coatings in 3.5 % NaCl.

Designing bi-metal and tri-metal oxide composite coatings is a highly effective approach to extending the lifespan of stainless steel [48]. The exceptional inhibition efficiency (IE %) of the Ni/GO/Fe-TiO_2 nanocomposite is primarily attributed to the presence of Fe_3O_4 nanoparticles. These nanoparticles exhibit strong superparamagnetic properties, photothermal capacity, chemical stability, and high loading efficiency [49, 50, 51]. Nanofillers with photothermal capacity can enhance the release of internal corrosion inhibitors [52] and enable the self-healing capabilities of the coating matrix through reversible chemical bonds [53, 54] or physical molecular arrangements [55, 56]. Consequently, the photothermal effect of Fe_3O_4 nanoparticles allows for the rapid self-healing of cracks in the composite film, ensuring its superior corrosion resistance and high inhibition efficiency.

3.5. Surface morphology

Fig. 9 shows the SEM image of the corroded T91 steel without coating after being immersed in 3.5 % NaCl at RT. The average pore size is about 349.3 nm. Fig. 10 shows the SEM image and EDX result of corroded T91 steel coated with Ni/GO/Fe-TiO_2 after being immersed in 3.5 % NaCl at RT. The pitting disappears due to coating before corrosion. It may be due to contains protective layers that reduce the corrosion of the steel. Coated with Ni/GO/Fe-TiO_2 prevents or decreases the CR of the T91 as in the image and confirmed by EDX analysis. A part of the coating is loose but still exists some of it is Ni, C, O, and Ti. In Figure 4 (d), the concentrations of chlorine and oxygen are reduced compared to the pre-corrosion state. Figure 9b provides a visual representation of the samples' condition after immersion for 120 h, illustrating significant variations in the extent of corrosion damage during this initial period. As immersion duration increased, there was a corresponding rise in the formation

of corrosion products on the untreated samples. Simultaneously, there was a decrease in the number of detached corrosion products, indicating a reduction in the rate of corrosion attack. However, corrosion products were present on the coated samples. Nevertheless, no corrosion products were detached during the immersion test, suggesting less severe corrosion. The SEM micrographs in Fig. 10a depict the morphology of the sample surfaces after removing the corrosion products. The coated sample exhibited significantly less severe and more consistent corrosion damage compared to the untreated sample.

The difference in the enhancement of corrosion resistance shown in electrochemical tests compared to immersion tests can be attributed to changes in surface properties during immersion and the difficulty of eliminating corrosion products. During the initial stages of immersion, untreated samples experienced a high CR, leading to rapid coverage of the surface with corrosion products, as depicted in Figure 6. This resulted in a decrease in the rate of subsequent corrosion attacks. It can be inferred that, at least initially, deposition-coated samples exhibited much higher resistance to corrosion compared to untreated samples. This aligns with the findings of electrochemical experiments, which evaluated short-term corrosion resistance levels. Based on the results of both electrochemical tests and immersion tests, it can be concluded that the coating initially provides a high level of protection. However, its effectiveness diminishes over time. The nanocomposite coating on T91 steel significantly improved corrosion resistance, as demonstrated by both electrochemical and immersion experiments in Hanks' solution, evident in terms of CR and the extent of damage.

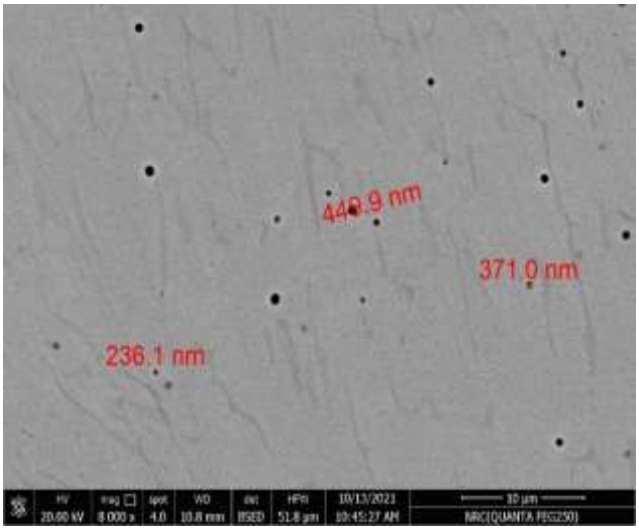

Fig. 9. The SEM image of T91 steel immersed in 3.5%NaCl at RT

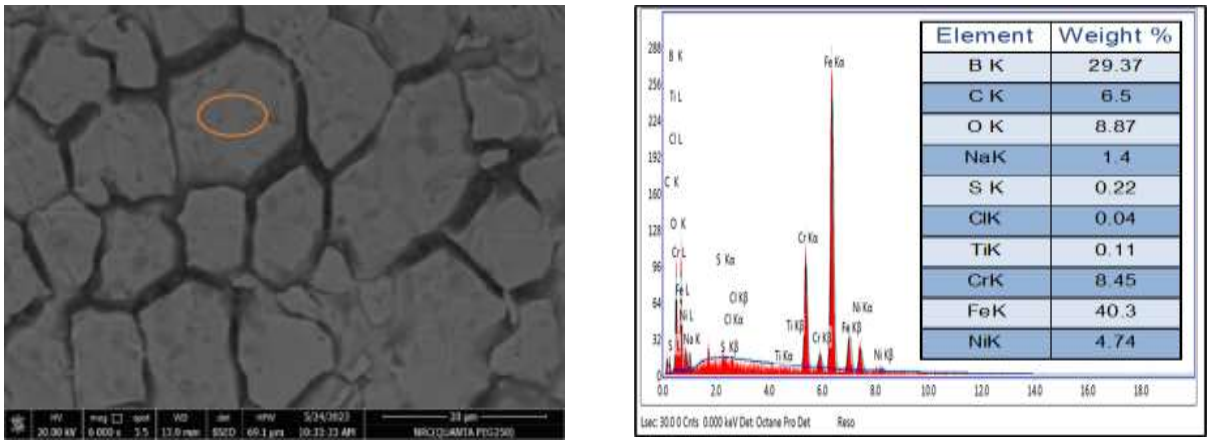

(a) **(b)**

Fig. 10. (a) The SEM image and (b) EDX result of coated T91 steel by Ni/GO/Fe-TiO_2 after being immersed in 3.5 % NaCl in RT.

3.6. Analysis of variance (ANOVA)

The F-test and p-value confirmed the statistical significance of the regression model. The ANOVA data for the response surface model (RSM) are presented in Table 5. Generally, the p-value is used to assess the significance of a coefficient, with smaller p-values indicating greater significance. Typically, a p-value less than 0.05 indicates the significance of the model terms [57]. As shown in Table 5, the p-value of the regression model is denoted with a single star, representing the highest significance level

and suggesting the significance of the model terms. Higher R^2 values indicate a closer match between predicted and experimental values. The predicted R^2 (97.55%) and adjusted R^2 (99.25%) values are in close agreement, indicating the accuracy of the model.

Table 5. ANOVA results for CR of T91 steel with and without nanocomposite deposition in 3.5%NaCl

Source	DF	Adj SS	Adj MS	F-Value	P-Value
Model	9	29.3807	3.26452	354.49	0.000
Linear	3	20.2050	6.73500	731.33	0.000
ID	1	0.0528	0.05275	5.73	0.030
Time (h)	1	3.0456	3.04559	330.71	0.000
WL (g)	1	1.4632	1.46317	158.88	0.000
Square	3	0.5766	0.19221	20.87	0.000
ID*ID	1	0.0320	0.03196	3.47	0.082
Time (h)*Time (h)	1	0.4590	0.45905	49.85	0.000
WL (g)*WL (g)	1	0.0297	0.02972	3.23	0.093
2-Way Interaction	3	1.0122	0.33741	36.64	0.0001
ID*Time (h)	1	0.0272	0.02724	2.96	0.106
ID*WL (g)	1	0.0003	0.00028	0.03	0.865
Time (h)*WL (g)	1	0.0043	0.00431	0.47	0.504
Error	15	0.1381	0.00921		
Total	24	29.5189			

where ID stands for T91 steel, Ni, Ni/TiO_2, Ni/GO/TiO_2, Ni/GO/Fe-TiO_2 bathes which correspond to No. 1-5.

The ANOVA Plots, including the main effect plot and interaction effect plot, are displayed in Fig. 11. The p-values obtained from the One-Way ANOVA indicate that they fall below the accepted threshold of 0.05. Additionally, the R-square value for the correlation between corrosion rate and time/weight is determined to be 98.92%. An observation from the data suggests that as immersion time increases, both weight loss and corrosion rate also increase.

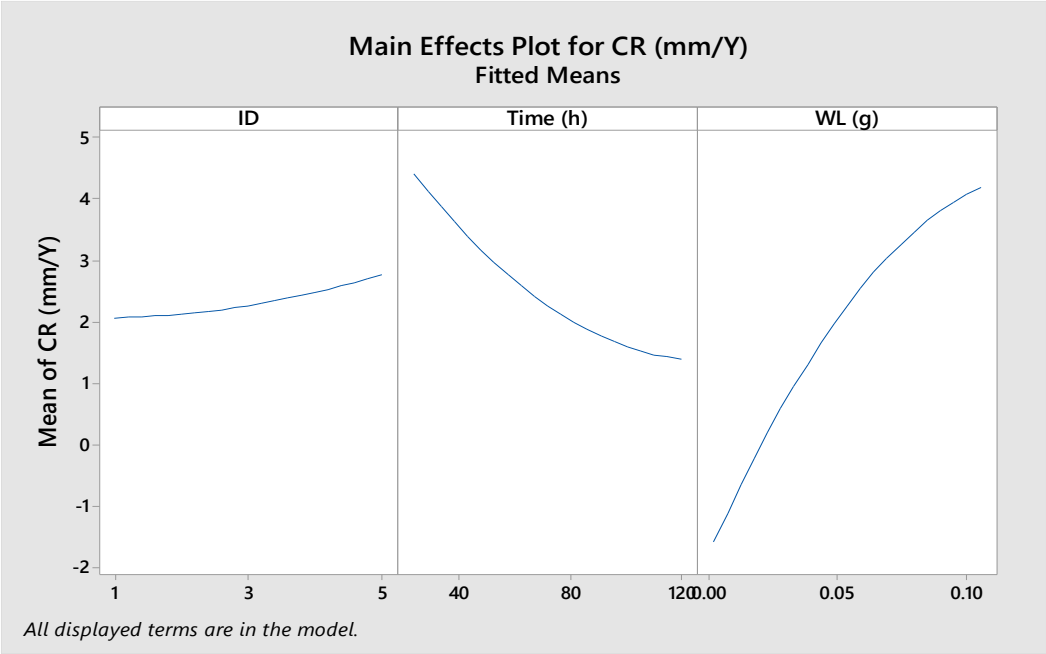

(a)

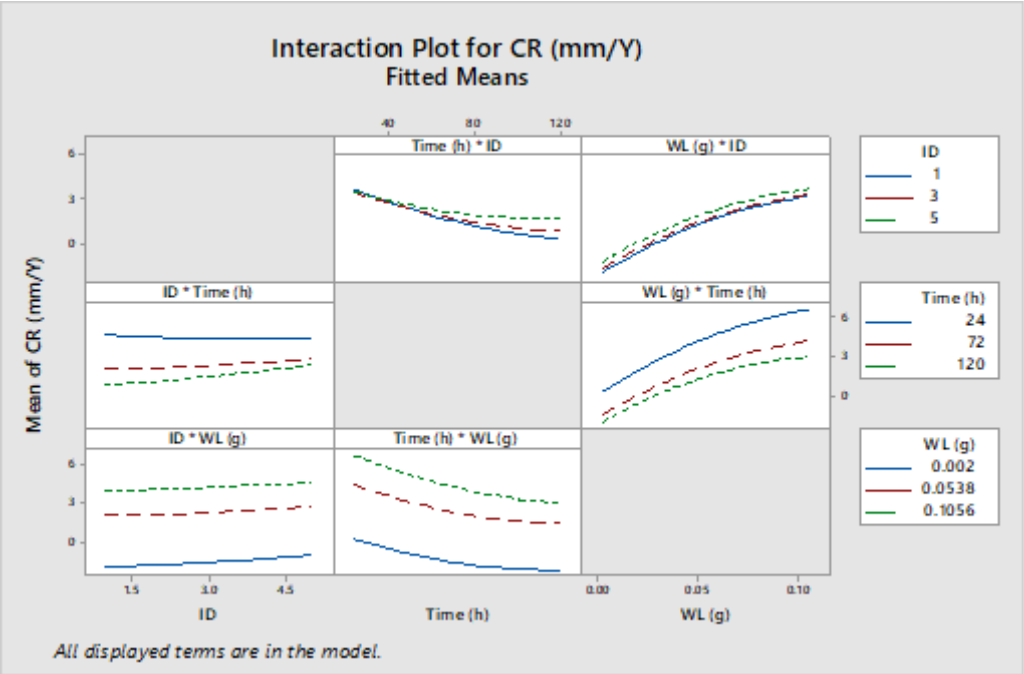

(b)

Fig. 11. ANOVA Plots for the mean values of CR: (a) Main effects plot, (b) Interaction plot.

In Fig. 12, the Pareto chart displays the standardized effects for the corrosion rate (CR) with a confidence level of 95%. The estimated regression coefficients in the model (5) for corrosion rate reveal the main effects of time, ID of coating, and WL on T91 steel. The p-values for these main effects are below the accepted threshold of 0.05, indicating their statistical significance. Additionally, the p-value for two-way interactions is 0.0001. The most significant effects are attributed to time, ID of coating, and weight loss, while the effects of other coefficients were found to be insignificant.

The R-squared (R^2) and adjusted R-squared (adj R^2) values for the CR regression models are 99.53% and 99.25%, respectively. A mathematical model (5) was developed to understand the effects of different variables and their interactions on the corrosion rate. As expected, increasing the immersion time leads to an increase in WL. This increase in WL corresponds to a higher corrosion rate for T91 steel. Additionally, response optimization for corrosion rate identified the maximum fit of 74.39% at a time of 24 h, with a weight loss of 0.00513 for ID 5 Ni/GO/Fe-TiO_2

Mathematical model for CR (mm/Y) = 2.066- 0.338 ID- 0.0776 Time (h)+ 106.4 WL (g) + 0.0364 ID*ID+ 0.000276 Time (h)*Time (h)- 361 WL (g)*WL (g)+ 0.00458 ID*Time (h)- 0.65 ID*WL (g)- 0.135 Time (h)*WL (g) (5)

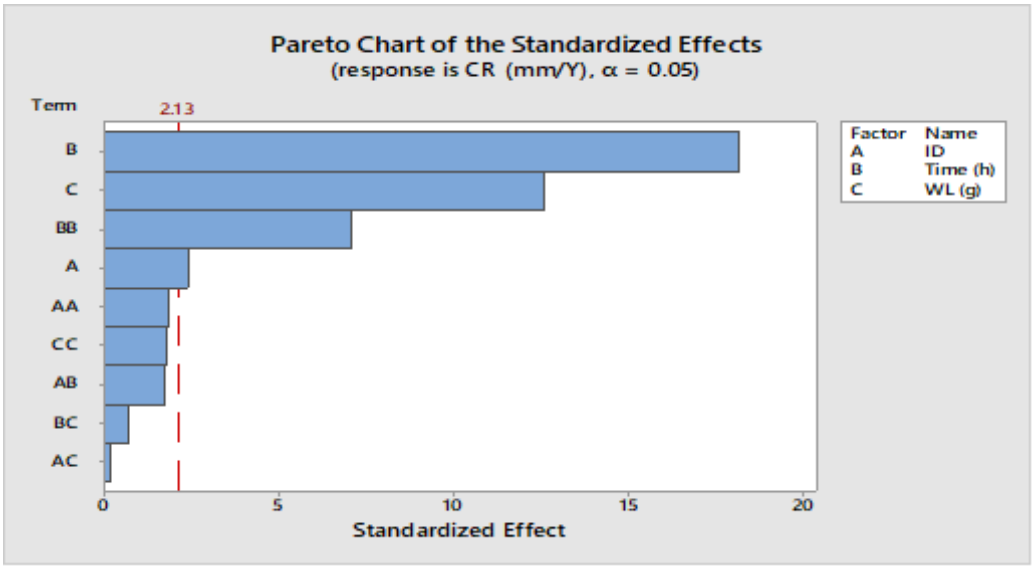

Fig. 12. Pareto chart of the standardized effect for CR of Cu45Mn25Al15Fe5Cr5Ni5 HEA.

4. Conclusions

The development of a graphene coating with high efficiency, stability, and low cost on the T91 steel substrate has long been anticipated, despite being a challenging task. In this study, an electrodeposition approach was employed to coat Ni-reduced graphene doped with Ni/GO/TiO_2 and GO/Fe-TiO_2 nanocomposite coatings onto T91. The resulting coating exhibits a gradient structure of graphene-CrC towards the outer surface. Characterization of the coated samples revealed enhanced corrosion resistance in a 3.5% NaCl, as observed through both gravimetric and electrochemical studies. Immersion experiments further demonstrated that the deposition-coated surfaces experienced less severe and more consistent corrosion attacks, evident from the appearance of the damaged surfaces. The CR value decreased by 0.854 mm/y, implying a significant improvement in corrosion resistance. This enhancement level surpasses or matches that of Ni/ TiO_2 and Ni/GO/TiO_2 nanocomposite coatings. The properties of deposition-coated surfaces were determined using XRD, SEM, and EDX analysis. RSM was utilized to optimize the corrosion rate of T91 steel, measured using the weight loss method. Additionally, response optimization for CR identified a maximum fit of 74.39% after 24 h, with a weight loss of 0.00513 for Ni/GO/Fe-TiO_2.

Conflict of interest

The authors report no conflicts of interest.

References

[1]. D. Dutta, A. N. F. Ganda, J. K. Chih, C. C. Huang, C. J. Tseng, C. Y. Su, Revisiting graphene-polymer nanocomposite for enhancing anticorrosion performance: A new insight into interface chemistry and diffusion model, Nanoscale, 10(26), 12612–12624, 2018.

[2]. S. Pourhashem, A. Rashidi, M. R. Vaezi, M. R. Bagherzadeh, Excellent corrosion protection performance of epoxy composite coatings filled with amino-silane functionalized graphene oxide, Surf. Coatings Technol., 317, 1–9, 2017.

[3]. M.C. Isa, A.R.A. Manaf, M.H. Anuar, Combating corrosion: risk identification, mitigation and management, Defence S and T Technical Bulletin 11(1):1-12, 2018.

[4]. M.Y. Rekha, C. Srivastava, Microstructure and corrosion properties of zinc-graphene oxide composite coatings, Corros. Sci., 152, 234–248, 2019.

[5]. J. A. Quezada-Renteria, L. F. Chazaro-Ruiz, J. R. Rangel-Mendez, Poorly conductive electrochemically reduced graphene oxide films modified with alkyne chains to avoid the corrosion-promoting effect of graphene-based materials on carbon steel, Carbon N. Y., 167, 512–522, 2020.

[6]. C. Garcia-Cabezon, C. Salvo-Comino, C. Garcia-Hernandez, M. L. Rodriguez-Mendez, F. Martin-Pedrosa, Nanocomposites of conductive polymers and nanoparticles deposited on porous material as a strategy to improve its corrosion resistance, Surf. Coatings Technol., 403, 126395, 2020.

[7]. M. Zhu, Z. Du, Z. Yin, W. Zhou, Z. Liu, S.H. Tsang, E.H.T. Teo, Low-Temperature in Situ Growth of Graphene on Metallic Substrates and Its Application in Anticorrosion, ACS Appl. Mater. Interfaces, 8(1), 502–510, 2016.

[8]. N. Yang, T. Yang, W. Wang, H. Chen, W. Li, Polydopamine modified polyaniline-graphene oxide composite for enhancement of corrosion resistance, J. Hazard. Mater., 377, 142–151, 2019.

[9]. B. Jin, D-B. Xiong, Z. Tan, G. Fan, Q. Guo, Y. Su, Z. Li, D. Zhang, Enhanced corrosion resistance in metal matrix composites assembled from graphene encapsulated copper nanoflakes, Carbon N. Y., 142, 482–490, 2019.

[10]. Y. Ye, D. Zhang, T. Liu, Z. Liu, J. Pu, W. Liu, H. Zhao, X. Li, L. Wang, Superior corrosion resistance and self-healable epoxy coating pigmented with silanzied trianiline-intercalated graphene, Carbon N. Y., 142, 164–176, 2019.

[11]. A. A. Javidparvar, R. Naderi, B. Ramezanzadeh, Epoxy-polyamide nanocomposite coating with graphene oxide as cerium nanocontainer generating effective dual active/barrier corrosion protection, Compos. Part B Eng., 172, 363–375, 2019.

[12]. R.W. Swindeman, M.L. Santella, P.J. Maziasz, B.W. Roberts, K. Coleman, Issues in replacing Cr–Mo steels and stainless steels with 9Cr–1Mo–V steel, International Journal of Pressure Vessels and Piping 81 (2004) 507–512.

[13]. K. S. Novoselov, A. K. Geim, S. V. Morozov, D. Jiang, Y. Zhang, S. V. Dubonos, I. V. Grigorieva, A. A. Firsov, Electric Field Effect in Atomically Thin Carbon Films, Science, (2004), 666-669.

[14]. J. Kang, S. Zhang, Z. Zhang, Three-Dimensional Binder-Free Nanoarchitectures for Advanced Pseudocapacitors, Adv. Mater., 29(48), 1–12, 2017.

[15]. W. Chang, P. Wang, Y. Zhao, C. Ren, B. N. Popov, C. Li, Characterizing corrosion properties of graphene barrier layers deposited on polycrystalline metals, Surf. Coatings Technol., 398, 126077, 2020.

[16]. Y-P. Hsieh, M. Hofmann, K-W. Chang, J.G. Jhu, Y-Y. Li, K.Y. Chen, C.C. Yang, W-S. Chang, L-C. Chen, Complete corrosion inhibition through graphene defect passivation, ACS Nano, 8(1), 443–448, 2014.

[17]. S. Rossi, F. Russo, N. Gasparre, V. Fontanari, Influence of graphene addition on the mechanical and surface properties of vitreous enamel coatings, Surf. Coatings Technol., 398, 126071, 2020.

[18]. J. Tian, S. Wu, X. Yin, W. Wu, Novel preparation of hydrophilic graphene/graphene oxide nanosheets for supercapacitor electrode, Appl. Surf. Sci., 496, 143696, 2019.

[19]. X. Yi, A. Ma, L. Zhang, Y. Zheng, In-situ growth of graphene on 90Cu10Ni by electron beam irradiation during EBSD and its anti-corrosion property, Surf. Coatings Technol., 398, 126076, 2020.

[20]. M. R. Anisur, P. Chakraborty Banerjee, C. D. Easton, R. K. Singh Raman, Controlling hydrogen environment and cooling during CVD graphene growth on nickel for improved corrosion resistance, Carbon N. Y., 127, 131–140, 2018.

[21]. Y. Wu, W. Zhao, X. Zhu, Q. Xue, Improving the corrosion resistance of graphene-coated copper via accurate defect healing without sacrificing electronic conductivity, Carbon N. Y., 153, 95–99, 2019.

[22]. X. Li, W. Cai, J. An, S. Kim, J. Nah, D. Yang, R. Piner, A. Velamakanni, I. Jung, E. Tutuc, S.K. Banerjee, L. Colombo, R. S Ruoff, Large-area synthesis of high-quality and uniform graphene films on copper foils, Science, 324(5932), 1312–1314, 2009.
[23]. H. Gullapalli, A. L. Mohana Reddy, S. Kilpatrick, M. Dubey, P. M. Ajayan, Graphene growth via carburization of stainless steel and application in energy storage, Small, 7(12), 1697–1700, 2011.
[24]. X. Feng, S. Maier, M. Salmeron, Water splits epitaxial graphene and intercalates, J. Am. Chem. Soc., 134(12), 5662–5668, 2012.
[25]. T. Yoon, W. C. Shin, T. Y. Kim, J. H. Mun, T. S. Kim, B. J. Cho, Direct measurement of adhesion energy of monolayer graphene as-grown on copper and its application to renewable transfer process, Nano Lett., 12(3), 1448–1452, 2012.
[26]. C. Cui, A. T. O. Lim, J. Huang, A cautionary note on graphene anti-corrosion coatings, Nat. Nanotechnol., 12(9), 834–835, 2017.
[27]. L. Lin, H. Peng, Z. Liu, Synthesis challenges for graphene industry, Nat. Mater., 18(6), 520–524, 2019.
[28]. M. A. Raza, Z. U. Rehman, F. A. Ghauri, A. Ahmad, R. Ahmad, M. Raffi, Corrosion study of electrophoretically deposited graphene oxide coatings on copper metal, Thin Solid Films, 620, 150–159, 2016.
[29]. D.M. Behunová, G. Gallios, V. Girman, H. Kolev, M. Kaňuchová, S. Dolinská, M. Václavíková, Electrophoretic deposition of graphene oxide on stainless steel substrate, Nanomaterials, 11(7), 1–16, 2021.
[30]. S. M. Park, J. S. Yoo, Electrochemical impedance spectroscopy for better electrochemical measurements, Anal. Chem., 75(21), 455–461, 2003.
[31]. N. T. Kirkland, T. Schiller, N. Medhekar, N. Birbilis, Exploring graphene as a corrosion protection barrier, Corros. Sci., 56, 1–4, 2012.
[32]. M. Fathy, A. Gomaa, F. A. Taher, M. M. El-Fass, A. E. H. B. Kashyout, Optimizing the preparation parameters of GO and rGO for large-scale production, J. Mater. Sci., 2016.
[33]. E. Kamal, G. Hamdy, I. A. El-Sabbagh, Highly efficient capture of Th(IV) from aqueous solutions using GO/TiO2 nanocomposite, Egypt. J. Chem., 64(3), 1353–1362, 2021.
[34]. E. Kamal, G. Hamdy, I. A. El-Sabbagh, F. A. Taher, Highly efficient sorption of thorium (IV) onto a ternary magnetic TiO2/Fe3O4/GO nanocomposite, Mater. Today Proc., 42, 2218–2226, 2021.
[35]. W. Nachit, S. Touhtouh, Z. Ramzi, M. Zbair, A. Eddiai, M. Rguiti, A. Bouchikhi, A. Hajjaji K. Benkhouja, Synthesis of nanosized TiO2 powder by sol gel method at low temperature, Mol. Cryst. Liq. Cryst., 627(1), 170–175, 2016.
[36]. L.Z. Mohamed, K.A. Abdelghafar, H. Ali, G.A. Gaber, Comparative Studies of Cr/Ti Additions for Cu40Mn25Al20Fe5Ni5 HEA on Microstructure and Corrosion Behavior in HNO3 Solution, International Journal of Metalcasting, 17(3):1791-1805, 2023
[37]. G.A. Gaber, L.Z. Mohamed, W. Abd-ElaAziem, Influence of Different Processes on Corrosion Performance of Al 1070 Alloy in Chloride Media, Egyptian Journal of Chemistry, Egypt. J. Chem., 67(9), 381-391, 2024.
[38]. G. Fadel, L.Z. Mohamed, G.A. Gaber, O. El kady, A. Elhabak, M. Adly, S.A. Abolkassem, Evaluation of corrosion and wear features of Al matrix reinforced with particles (SiC+Y2O3) coated with either nano-Ag/Ni or nano/Ag/Cu, Egypt. J. Chem., 67(8), 137–155, 2024.
[39]. O. Sadek, S. Touhtouh, E. Mahdi Bouabdalli, A. Hajjaji, Development of a protocol for the rapid identification of solid materials using the principal component analysis (ACP) method: Case of phosphate fertilizers, Mater. Today Proc., 66, 402–407, 2022.
[40]. B. Himabindu, N. S. M. P. Latha Devi, B. Rajini Kanth, Microstructural parameters from X-ray peak profile analysis by Williamson-Hall models; A review, Mater. Today Proc., 47, 4891–4896, 2021.
[41]. C. Zhang, S. Zhang, D. Sun, J. Lin, F. Meng, H. Liu, Superhydrophobic fluoride conversion coating on bioresorbable magnesium alloy – fabrication, characterization, degradation and cytocompatibility with BMSCs, J. Magnes. Alloy., 9(4), 1246–1260, 2021.
[42]. A. Ghanbari, M. M. Attar, The effect of zirconium-based surface treatment on the cathodic disbonding resistance of epoxy coated mild steel, Appl. Surf. Sci., 316(1), 429–434, 2014.
[43]. L.A. Hernandez-Alvarado, L.S. Hernandez, S.L. Rodriguez-Reyna, Evaluation of corrosion behavior of galvanized steel treated with conventional conversion coatings and a chromate-free organic inhibitor, Int. J. Corros., 2012.
[44]. M. M. Abou-Krisha, A. G. Alshammari, F. H. Assaf, F. A. El-Sheref, Electrochemical behavior of Zn–Co–Fe alloy electrodeposited from a sulfate bath on various substrate materials, Arab. J. Chem., 12(8), 3526–3533, 2019.
[45]. A.T. Smith, A.M. LaChance, S. Zeng, B. Liu, L. Sun, Synthesis, properties, and applications of graphene oxide/reduced graphene oxide and their nanocomposites, Nano Materials Science 1 (2019) 31-47
[46]. S. Sadhukhan, T.K. Ghosh, D. Rana, I. Roy, A. Bhattacharyya, G. Sarkar, M. Chakraborty, D. Chattopadhyay, Studies on synthesis of reduced graphene oxide (RGO) via green route and its electrical property, Materials Research Bulletin, 79 (2016) 41-51.
[47]. S. Jin, V. H. Pham, J. H. Dickerson, M. Brochu, Interfacial Development of Electrophoretically Deposited Graphene Oxide Films on Al Alloys, J. Electrochem. Soc., 162(11), D3025–D3029, 2015.
[48]. S. Mandal, V. Das, M. Debata, A. Panigrahi, P. Sengupta, A. Rajendran, D. Pattanayak S. Basu, Study of pore morphology, microstructure, and cell adhesion behaviour in porous Ti-6Al-4V scaffolds, *Emergent Mater.*, 2019, **2**, 453–462.
[49]. H. Zhang, B. Lin, J. Tang, Y. Wang, H. Wang, H. Zhang, J. Cao, J. Hou. M. Sun, H. Zhang, An ethyl cellulose-based supramolecular gel composite coating for metal corrosion protection and its self-healing property from electromagnetic heating effect, Surf. Coat. Technol. 424 (2021) 127647.
[50]. A. Ma, J. Wei, Y. Wu, Y. Wu, W. Zhao, A novel directional repairing rGO-Fe_3O_4/Oil coating with magnetic driving for metal protection and self-healing, Chem. Eng. J. 421 (2021) 129597.

[51]. X. Liu, J. Wang, W. Hu, Synthesis, inhibition behavior and recycling of Fe_3O_4 @ZnAl-MoO_4 LDH nanocomposite inhibitor, J. Alloy. Compd. 801 (2019) 489–501.
[52]. L. Ma, J. Wang, D. Zhang, Y. Huang, L. Huang, P. Wang, H. Qian, X. Li, H.A. Terryn, J. Mol, Dual-action self-healing protective coatings with photothermal responsive corrosion inhibitor nanocontainers, Chem. Eng. J. 404 (2021) 127118.
[53]. Y. Ma, Y. Yang, D. Cao, J. Fang, C. Zhu, M. Yang, L. Fang, C. Lu, Z. Xu, Facile repair of anti-corrosion polymeric composite coatings based on light triggered self-healing, Macromol. Mater. Eng. 306 (9) (2021) 2100106.
[54]. Y. Zou, L. Fang, T. Chen, M. Sun, C. Lu, Z. Xu, Near-infrared light and solar light activated self-healing epoxy coating having enhanced properties using MXene flakes as multifunctional fillers, Polymers-Basel 10 (2018) 474.
[55]. L. Ma, X. Wang, J. Wang, J. Zhang, C. Yin, L. Fan, D. Zhang, Graphene oxide-cerium oxide hybrids for enhancement of mechanical properties and corrosion resistance of epoxy coatings, J. Mater. Sci. 56 (2021) 10108–10123.
[56]. C. Ren, Y. Huang, W. Hao, D. Zhang, X. Luo, L. Ma, J. Wang, T. Chowwanontha-punya, C. Dong, X. Li, Multi-action self-healing coatings with simultaneous recovery of corrosion resistance and adhesion strength, J. Mater. Sci. Technol. 101 (2021) 18–27.
[57]. G. Tansuğ, T. Tüken, N. Kıcır, M. Erbil, Investigation of 2-aminoethanethiol as corrosion inhibitor for steel using response surface methodology (RSM). Ionics, (2014) 20(2):287–294.